



HAL
open science

Assessing carbon or tungstates coverage of ZrO₂ nanoparticles supported on MWCNT via NO_x-TPD

Patrick Kelleher, Gary Haller, Sandra Casale, Christophe Méthivier, Cyril Thomas

► **To cite this version:**

Patrick Kelleher, Gary Haller, Sandra Casale, Christophe Méthivier, Cyril Thomas. Assessing carbon or tungstates coverage of ZrO₂ nanoparticles supported on MWCNT via NO_x-TPD. *Nano-Structures & Nano-Objects*, 2018, 16, pp.110-119. 10.1016/j.nanoso.2018.05.003 . hal-01803349

HAL Id: hal-01803349

<https://hal.sorbonne-universite.fr/hal-01803349>

Submitted on 22 Jun 2018

HAL is a multi-disciplinary open access archive for the deposit and dissemination of scientific research documents, whether they are published or not. The documents may come from teaching and research institutions in France or abroad, or from public or private research centers.

L'archive ouverte pluridisciplinaire **HAL**, est destinée au dépôt et à la diffusion de documents scientifiques de niveau recherche, publiés ou non, émanant des établissements d'enseignement et de recherche français ou étrangers, des laboratoires publics ou privés.

Assessing Carbon or Tungstates Coverage of ZrO₂ Nanoparticles Supported on MWCNT *via* NO_x-TPD

**Patrick R. Kelleher,¹ Gary L. Haller,¹ Sandra Casale,² Christophe Méthivier,² and
Cyril Thomas^{2,*}**

1- Department of Chemical and Environmental Engineering, Yale University, New Haven,
CT, 06520, USA

2- Sorbonne Université, UPMC Univ Paris 06, UMR CNRS 7197, Laboratoire de Réactivité
de Surface, 4 Place Jussieu, Tour 43-53, 3^{ème} étage, Case 178, F-75252, Paris, France

*Corresponding author. E-mail: cyril.thomas@upmc.fr (Cyril Thomas)

Tel: + 33 1 44 27 36 30 / Fax: + 33 1 44 27 60 33

Abstract:

Multi-walled carbon nanotubes (MWCNT) promoted by oxides, that are far from trivial to characterize, have emerged as promising candidates in several fields such as biosensors and catalysis. In this study the coverage of ZrO_2 nanoparticles supported on MWCNT, by carbonaceous deposits or tungstates was investigated by NO_x temperature-programmed desorption (NO_x -TPD). ZrO_2 coverage by carbonaceous deposits was found to be about 30 %, whereas that by tungstates varied from 40 to 77 % depending on the W loading of the sample. The size of the ZrO_2 particles estimated by NO_x -TPD (~ 2.3 nm) was found to be in excellent agreement with that determined by TEM. Remarkably, it was found that W interacted preferentially with the ZrO_2 nanoparticles for a W surface density of $1.9 \text{ W/nm}^2_{\text{ZrO}_2}$ (half monolayer coverage of the ZrO_2 nanoparticles by tungstates). Monolayer coverage of ZrO_2 by tungstates was nearly complete when introducing a W loading twice as high as that theoretically needed. These insights into the surface coverage of ZrO_2 by carbon or tungstates could not be obtained by any means other than NO_x -TPD, which makes it a unique method to provide advanced characterization of the surface of oxides supported on MWCNT, in particular, and carbon supports, to a broader general interest.

Keywords: Multi-walled Carbon Nanotubes (MWCNT); Tungstated-zirconia; NO_x -TPD; TEM; XPS

1. Introduction

Since the original discovery of carbon nanotubes (CNT) by Ijima in the early nineties [1] the properties of these materials have been extensively studied in various fields [2-5]. In the catalysis domain, CNT and multi-walled carbon nanotubes (MWCNT) have been suggested to be promising catalyst supports or promoters, in particular when modified with metals and/or oxides [6,7]. Regarding the modification of MWCNT by addition of ZrO_2 , very few studies have been reported in the literature to our knowledge [8-20], although ZrO_2 has long been of interest in catalysis [21], in particular for acid-catalyzed reactions when promoted by sulfates [22] and tungstates (WO_x) [23-25]. Characterization of the ZrO_2 -modified MWCNT materials has been carried out by electron microscopies [8-11,13,15,16,18-20,26] and XRD [8-13,15,16,18,20,26], as long as crystalline ZrO_2 particles are large enough for detection. From these studies it can be concluded that the size of the ZrO_2 particles were rather widespread [9-11] and higher than or equal to 10 nm in the majority of the synthesized samples [8,9,11,13,18,19]. Recently we proposed that narrowly distributed, highly dispersed, ZrO_2 nanoparticles (2-3 nm) could be obtained by grafting zirconium acetylacetonate ($\text{Zr}(\text{acac})_4$) on MWCNT that were previously functionalized in nitric acid [14-17].

Although estimating the size of the ZrO_2 nanoparticles by XRD and TEM remains reliable, these physical methods are limited when interest lies in characterization of their surface, which is of fundamental importance when a catalytic application is considered. Recently, we have shown that the accessible surface of ZrO_2 in complex materials can be accurately estimated with the use of a novel chemisorption technique, namely the adsorption of nitrogen oxides ($\text{NO}_x = \text{NO} + \text{NO}_2$) at RT followed by their temperature-programmed desorption (NO_x -TPD) [27,28]. Thus, we have found of particular interest to characterize the

size and accessible surface of ZrO₂ nanoparticles supported on MWCNT (ZrO₂/MWCNT) by this newly-developed technique.

The aforementioned ZrO₂/MWCNT composite has been further functionalized by adding W to make tungsten-promoted ZrO₂ nanoparticles supported on MWCNT (WO₃-ZrO₂/MWCNT). Due to their intrinsic acid properties, tungstated zirconias have attracted the attention of the catalysis community for about three decades [29]. Several studies have shown that the W surface density (W/nm²), also reflecting the coverage of ZrO₂ by tungstates [30,31], is the critical parameter when determining performance of these catalysts in various catalytic reactions [25,29]. Consequently, much work has been devoted to determining the W surface density for which monolayer coverage of WO_x on a ZrO₂ support is achieved.

Physical probes such as Raman [31,32-34], Ion Scattering [35] and X-ray Photoelectron [36-40] spectroscopies have proven to be useful when characterizing bulk tungstated zirconias, however, there is inherent difficulty when using Raman spectroscopy to characterize lowly-loaded samples, such as the WO₃-ZrO₂/MWCNT samples described in this study. Furthermore, Ion Scattering and X-ray Photoelectron spectroscopies (ISS and XPS) are not readily available to all scientists characterizing these types of materials and this offers potential for new methods that are capable of characterizing these complex materials. The adsorption of chemical probes such as CO and CO₂ followed by FT-IR (CO [41]) or volumetric analysis (CO [35,41], CO₂ [31]) has also been used to characterize the coverage of ZrO₂ by tungstates. FT-IR becomes less favorable when a carbon support is introduced due to carbon absorbing the IR beam. In addition, the dependence of CO and CO₂ adsorption on the nature of the ZrO₂ polymorph being investigated [42] increases the uncertainty in methods relying on CO and CO₂ adsorption. For these reasons, the WO₃-ZrO₂/MWCNT samples in the current study were characterized by NO_x-TPD to determine the coverage of the ZrO₂ nanoparticles by tungstates. It is our understanding that NO_x-TPD can be performed by

scientists everywhere and on tungstated zirconia samples of any composition, making it a sensitive and robust technique to determine the W surface density on ZrO₂ supports. To our knowledge, determination of the coverage of the ZrO₂ surface by tungstates in WO₃-ZrO₂/MWCNT materials has not been reported in the literature to date, whereas their use as substitutes of sulfated ZrO₂ materials, which are known to exhibit leaching issues in biomass processing applications[43-50], is of great interest.

2. Experimental

2.1. Catalyst preparation

The MWCNT used in this study were purchased from Cheap Tubes Inc. (>95% purity). These MWCNT (or pristine MWCNT, as described later) have an outer diameter of 10–20 nm, an inner diameter of 3–5 nm, and a length of 10–30 μm, as described by the supplier. The pristine MWCNT were functionalized by refluxing in nitric acid at ~120 °C for 2 h using ~69 wt % (15 M HNO₃) nitric acid (purchased from J.T. Baker). The mixture was then filtered and washed with 1000 mL of deionized water in five batches (5 × 200 mL) to remove excess acid and soluble oxidation products. The resulting material was then dried at 60 °C overnight in a thermostated oven and ground to a fine powder. These functionalized MWCNT were used as the starting material to prepare the ZrO₂/MWCNT composites.

Synthesis of ZrO₂/MWCNT was completed by grafting Zr(acac)₄ (98%, purchased from Sigma-Aldrich) onto functionalized MWCNT in refluxing toluene (300 mL) at ~111 °C for 3 h in a 500 mL round-bottom flask being purged with N₂ (ultrahigh purity, purchased from Airgas). The sample was filtered, washed three times with toluene, and dried overnight at 60 °C. A thermal treatment (annealing) was then performed in flowing He (ultrahigh purity, purchased from Airgas) at 450 °C for 2 h in a quartz reactor to decompose

the acetylacetonate precursor and form ZrO₂ particles. Two batches of ZrO₂/MWCNT were prepared differing in the loading of ZrO₂ (8.1 and 6.8 wt %) and the starting functionalized MWCNT. From here on, these samples will be denoted as ZrO₂(*x*)/MWCNT, where *x* represents the ZrO₂ loading (wt %).

The ZrO₂(6.8)/MWCNT composite was then impregnated with aqueous solutions of ammonium metatungstate hydrate (99.99%, purchased from Sigma-Aldrich) prepared at various concentrations to achieve WO₃ loadings of 2.33, 4.57 and 8.74 wt %. The impregnated material was thermally treated again at 450 °C in flowing He for 2 h in order to form tungstated ZrO₂/MWCNT (WO₃-ZrO₂/MWCNT). The tungstated samples will be denoted as WO₃(*y*)-ZrO₂(*x*)/MWCNT, where *y* and *x* represent the loadings (wt %) of WO₃ and ZrO₂, respectively. Note that when ZrO₂/MWCNT of *x* wt% is tungstated, the wt% ZrO₂ is adjusted to *x*' < *x* to account for the added WO₃, e.g., ZrO₂(6.8)/MWCNT becomes WO₃(2.3)-ZrO₂(6.6)/MWCNT.

2.2. Characterization Techniques

The samples were characterized by thermogravimetric analysis (TGA), X-ray diffraction (XRD), transmission electron microscopy (TEM), X-ray Photoelectron Spectroscopy (XPS) and NO_x-temperature-programmed desorption (NO_x-TPD).

Thermogravimetric Analysis (TGA). The final weight loadings of ZrO₂ and WO₃ were measured using TGA which was conducted on a Setaram Setsys 1750 instrument in flowing air (Ultra Zero grade, purchased from Airgas). During the measurement, the temperature was held at 200 °C for 30 min to remove adsorbed water and ramped to 1000 °C at a rate of 10 °C/min and then held at 1000 °C for 30 min. A second ramp on the oxidized sample was repeated to establish the baseline.

X-ray Diffraction Analysis (XRD). XRD patterns were collected using a Rigaku Miniflex 600 powder X-ray diffractometer with Cu K α radiation at $\lambda = 0.154$ nm. XRD data was collected in the range $2\Theta = 10 - 80^\circ$ with a continuous scan mode at $0.5^\circ/\text{min}$ and counts recorded every 0.02° . The XRD patterns have been scaled to the MWCNT (002) diffraction peak to clearly depict differences in each sample.

Transmission Electron Microscopy (TEM). Bright field TEM was performed at the Plate-forme of Institut des Matériaux de Paris Centre using a JEOL 2010 microscope operating at 200 kV with a LaB₆ filament and equipped with an Orius CCD camera (Gatan). The TEM samples were prepared by dropping ethanol suspensions of the materials on a copper grid. The ZrO₂ particle-size distributions were estimated by counting from 497 to 1133 particles.

X-ray Photoelectron Spectroscopy (XPS). XP spectra were collected on an Omicron Argus X-ray photoelectron spectrometer, using a monochromated Al K α ($h\nu = 1486.6$ eV) radiation source having a 300 W electron beam. Photoelectrons emitted from the sample were analyzed at a takeoff angle of 45° under ultra-high vacuum conditions (1×10^{-8} Pa). XP spectra were collected at a pass energy of 20 eV with 0.1 eV steps. After data collection, the binding energies were referenced to the C 1s line (284.5 eV). The peak areas were determined after subtraction of a Shirley background and the atomic ratio calculations were performed after normalization using Scofield factors. Spectrum processing was carried out using the Casa XPS software package and Origin 7.1 (Origin Lab Corporation).

NO_x Temperature-Programmed Desorption (NO_x-TPD). The NO_x-TPD experiments were carried out in a U-shape quartz reactor (15 mm i.d.). The samples were held on a plug of quartz wool and the temperature was controlled by a Eurotherm 2408 temperature controller using a K-type thermocouple. Reactant gases, used as received, were fed from independent gas cylinders (purchased from Air Liquide) by means of mass flow controllers (Brooks

5850TR) with a total flow rate of 230 mL_{NTP}/min. Due to the presence of the MWCNT support, and its known sensitivity to oxidation at high temperature in the presence of O₂ [9], the pretreatment and desorption feeds were modified compared to those used in our earlier studies [27,28]. O₂ was removed from these feeds and replaced with He to maintain identical flow rates. It was verified on a bulk ZrO₂ sample tested earlier (ZrO₂-600 fa [27]), that replacing the O₂-He pretreatment and desorption feeds with He did not alter the desorption profiles (not shown) or the amount of NO_x desorbed (475.5 μmol/g compared to 445.5 μmol/g [27]). Prior to the NO_x-TPD experiments, the MWCNT samples (~0.15 g) were annealed in situ in He at 500 °C (3 °C/min) for 2 h with a flow rate of 100 mL_{NTP}/min. Following the in-situ annealing, the sample was exposed to the adsorption mixture which consisted of 400 ppm NO_x (mainly NO with some NO₂) in He. The reactor outlet was continuously monitored by a chemiluminescence NO_x analyzer (Thermo Environmental Instruments 42C-HL) that allowed the simultaneous detection of both NO and NO₂. The samples were exposed to the adsorption mixture at RT until the outlet NO_x readout was equivalent to the inlet NO_x readout. This latter parameter was set to ensure that each sample was saturated under the present experimental conditions. The time after which no change was observed in the gas phase NO_x concentration was strongly dependent on the W surface density of the samples. It has been clearly demonstrated that the nature of formed ad-NO_x species on such materials is affected to a significant extent by the presence of O₂ in the NO-containing mixture [51]. As the presence of ppm levels of O₂ could not be excluded, NO_x adsorption was thus carried out in the presence of a large excess of O₂ (8 %). Before the NO_x-TPD experiments, the samples were flushed in He at RT to remove weakly chemisorbed species until the NO and NO₂ concentrations detected at the outlet of the reactor were found to be negligible. NO_x-TPD experiments were carried out from RT to about 400 °C at a heating rate of 3 °C/min under a flow of 230 mL_{NTP}/min of He. After each NO_x-TPD experiment, the NO_x analyzer was calibrated with a

NO/He standard mixture containing 933 ppm of NO. As reported earlier [27,52,53], it should be noted that NO_x chemisorption does not occur on WO_x species. The reactor outflow was also analyzed periodically using a μ-GC (Agilent Technologies, CP4900) equipped with a 5A molecular sieve column (80 °C, 150 kPa He, 200 ms injection time, 30 s backflush time) and a poraplot Q column (60 °C, 150 kPa He, 200 ms injection time). Under the NO_x-TPD conditions, the only detected product was CO₂ at ppm levels on the second column. The NO_x and CO₂ amounts were deduced from the integration of the corresponding TPD profiles. For the ZrO₂-containing materials, the amount of NO_x released per g of ZrO₂ was obtained by correcting the amount of NO_x released per g of sample for the amount of WO₃ and/or the background contribution of the MWCNT support.

3. Results and Discussion

3.1. MWCNT supports

TEM images show the MWCNT diameter's range from 9 to 24 nm and wall thicknesses of 5 ± 2 nm (Fig. 1a), consistent with the specifications indicated by the provider. Prior to studying the WO₃-ZrO₂/MWCNT materials, the corresponding MWCNT supports were submitted to NO_x-TPD experiments. As indicated in Fig. 2, which displays the NO_x and CO₂ profiles recorded in the course of a NO_x-TPD experiment carried out on the functionalized MWCNT support used for the preparation of ZrO₂(8.1)/MWCNT, the carbon support releases measurable amounts of NO_x from 50 to 400 °C with a maximum at 80 °C. The NO_x species are mainly released as NO except at low temperatures for which NO₂ is the dominant species. The production of CO₂ increased monotonously as the temperature increased. From a quantitative point of view, the amounts of NO_x released and CO₂ produced were found to be 58 and 41 μmol/g_{MWCNT}, respectively.

Two successive NO_x-TPD experiments, with intermediate annealing at 500 °C for 2 h under He, were also performed on the functionalized MWCNT support used for the preparation of ZrO₂(6.8)/MWCNT. The NO_x and CO₂ profiles (not shown) were found to be similar to those reported in Fig. 2. The amounts of NO_x released and CO₂ produced in these successive experiments were found to be reproducible ($70 \pm 4 \mu\text{mol NO}_x/\text{g}_{\text{MWCNT}}$ and $54 \pm 0 \mu\text{mol CO}_2/\text{g}_{\text{MWCNT}}$) and slightly higher than those obtained on the first batch of functionalized MWCNT investigated in this work (Table 1).

3.2. ZrO₂(8.1)/MWCNT

In agreement with our earlier studies [15,16], TEM images show that the outer surface of the MWCNT becomes uniformly decorated with ZrO₂ nanoparticles after grafting with Zr(acac)₄ and annealing in He (ZrO₂(8.1)/MWCNT, Fig. 1b). The ZrO₂ particle size distribution of this sample was found to be rather narrow (Fig. 1c) and the average ZrO₂ particle size was estimated to be 2.1 nm. This average size is consistent with our earlier work in which it was found that sintering of the ZrO₂ particles only occurred for highly-loaded samples and when thermally treated at high annealing temperatures [15]. The lower ZrO₂ particle density observed in Fig. 1b compared to those observed earlier [15] is also consistent with the lower ZrO₂ loading used in the present study. Fig. 1d,e indicate that the particle size was hardly affected after four successive NO_x-TPD experiments, as the average particle size was estimated to be 2.3 nm for this particular sample. In these NO_x-TPD experiments the annealing temperature never exceeded 500 °C and this result is in agreement with the finding that limited sintering of the ZrO₂ particles supported on MWCNT was previously reported for annealing temperatures lower than or equal to 550 °C [15].

Four NO_x-TPD experiments were performed successively on ZrO₂(8.1)/MWCNT (Fig. 3). Prior to each NO_x-TPD experiment, the sample was annealed in He for 2 h at 500 °C

following the original pretreatment procedure (100 mL/min He, 3 °C/min ramping rate). It must be highlighted however that this pretreatment was slightly modified after the third NO_x-TPD experiment as we anticipated that it would be of interest to monitor the CO₂ production in the course of the annealing treatment. For this purpose, the He flow rate was changed from 100 to 230 mL/min at 150 °C and the annealing treatment was performed under these particular conditions from 150 to 500 °C before carrying out the fourth NO_x-TPD experiment. Fig. 3a shows that the NO_x-TPD profiles obtained for ZrO₂(8.1)/MWCNT are significantly different from that obtained on MWCNT (Fig. 2). The NO_x contribution near 85 °C is of slightly higher intensity and an intense NO contribution is observed close to 290 °C on ZrO₂(8.1)/MWCNT when compared to blank MWCNT (Fig. 2). The NO_x-TPD profiles, corrected for the contribution of the MWCNT support (not shown), are found to be qualitatively consistent with that found on bulk ZrO₂ with low and high NO_x temperature desorption peaks [27]. Fig. 3a-d show an increase in the formation of NO₂ in the low-temperature desorption peak and a change in the shape of the NO_x peak as the number of successive NO_x-TPD experiments increases, in particular for the third and the fourth NO_x-TPD experiments (Fig. 3c,d). This change is clearly illustrated in Fig. 4a in which an increase in the intensity of the low temperature NO_x desorption peak can be easily observed for temperatures higher than 85 °C. Let us note that the shape of the low-temperature NO_x desorption peak recorded in the third and the fourth NO_x-TPD experiment (Fig. 4a) is closer to that reported earlier on bulk ZrO₂ [27] than those recorded in the two first NO_x-TPD experiments. The main difference between bulk ZrO₂ and ZrO₂(8.1)/MWCNT is related to the nature of the NO_x species released. Whereas NO₂ was found to primarily be released from bulk ZrO₂ [27], NO was almost exclusively released from ZrO₂(8.1)/MWCNT (Fig. 3). Before discussing this difference, it is interesting to note that an intense CO₂ contribution was observed in parallel with the NO contribution at 290 °C (Fig. 3) and that this CO₂ contribution

was only recorded in the NO_x-TPD experiments. Pretreatment of ZrO₂(8.1)/MWCNT under He only showed the presence of a CO₂ background from 150 to 500 °C (Fig. 4b, black trace). The nature of the NO_x adsorbed species (NO⁺, NO₂⁻, N₂O₃, N₂O₄, NO₃⁻) at the origin of the NO_x released at low temperatures on bulk ZrO₂ remains complex [54], whereas those responsible for the release of NO₂ at high temperatures have been attributed unequivocally to nitrates (NO₃⁻) [54-57]. The observed release of NO at high temperatures, instead of NO₂ as expected from the experiments carried out on bulk ZrO₂ [27] can thus be attributed to the reduction of NO₂ to NO assisted by the concomitant oxidation of the MWCNT support ($y \text{ NO}_2 + * \text{CO}_x = y \text{ NO} + \text{CO}_2$, where $x + y = 2$ and *C designates a carbon atom from MWCNT), in agreement with the conclusions drawn in the field of automotive exhaust soot oxidation [58-59]. Such an attribution is supported by the much greater CO₂ production observed for ZrO₂(8.1)-MWCNT (Fig. 4b) compared to MWCNT (Fig. 2).

Of much more interest is the evolution of the amounts of NO_x released and CO₂ produced in the successive NO_x-TPD experiments reported in Fig. 3 and Fig. 4. Overall, an increase in the amounts of NO_x released and CO₂ produced was observed from 220 to 286 μmol NO_x/g_{sample} and from 164 to 210 μmol CO₂/g_{sample}, respectively, as the number of NO_x-TPD experiment increased (Table 1). It must be emphasized that the increase in the amounts of NO_x released and CO₂ produced in the NO_x-TPD experiments were found to be more pronounced for the third experiment and seemed to stabilize after 3 consecutive NO_x-TPD experiments (Table 1). By correcting the amount of NO_x released per g of sample for the contribution of the MWCNT support (58 μmol NO_x/g_{MWCNT}), the amount of NO_x released per g of ZrO₂ was deduced to increase from 2063 to about 2834 μmol NO_x/g_{ZrO2} as the number of successive NO_x-TPD cycles increased (Table 1). Given that the NO_x surface density on ZrO₂ was determined to be 6 μmol NO_x/m²_{ZrO2} [27,28], the accessible surface of the ZrO₂

nanoparticles of ZrO₂(8.1)/MWCNT was determined to increase from 344 to about 470 m²/g_{ZrO₂} as the number of successive NO_x-TPD cycles increased (Table 1). This indicates that the accessible surface of the ZrO₂ nanoparticles increased after three successive NO_x-TPD experiments and then stabilized. By considering spherical ZrO₂ nanoparticles and a ZrO₂ density of 5.8 x 10⁶ g/m³, the size of the corresponding particles was estimated to decrease from 3.0 to 2.2 nm as the number of successive NO_x-TPD increased (Table 1). TEM showed that the size of the ZrO₂ particles was hardly affected by successive NO_x-TPD experiments and remained close to 2.2 nm (Table 1, Fig. 1b-e). The apparent decrease in the size of the ZrO₂ particles estimated from the NO_x-TPD data can be assigned to the occupation of the NO_x adsorption sites on the ZrO₂ particles by carbonaceous deposits that were progressively oxidized by NO₂ in the course of the successive NO_x-TPD experiments. The surface coverage of the ZrO₂ particles by these carbonaceous deposits is estimated to be about 30 %. It should be noted that the source of the carbonaceous deposits is likely the acetylacetonate decomposition of the zirconium precursor, not the MWCNT. From the fact that after four cycles the catalyst continues to produce significant quantities of CO₂ (Fig. 3d), it can be concluded that most of the CO₂ produced in the successive NO_x-TPD experiments (Fig. 3) is a result of oxidation of the MWCNT support by NO₂ released from the ZrO₂ particles, as discussed previously. This series of NO_x-TPD experiments was duplicated on a second aliquot of ZrO₂(8.1)/MWCNT and the results obtained were found to be fairly reproducible with the NO_x-TPD data reported in Fig. 3 and Table 1. Finally, it is of particular interest to highlight that the size of the ZrO₂ particles, freed of their initial C deposits, in ZrO₂(8.1)/MWCNT estimated by NO_x-TPD was found to be in remarkable agreement with the size of the ZrO₂ particles estimated by TEM (3rd and 4th NO_x-TPD, Table 1, 2.2 nm).

3.3. ZrO₂(6.8)/MWCNT

TEM indicates the ZrO₂(6.8)/MWCNT and ZrO₂(8.1)/MWCNT samples contain ZrO₂ particles of similar size (Fig. 1f,g, ~2.2 nm). In addition, the NO_x and CO₂ profiles recorded in the three successive NO_x-TPD experiments (Fig. 5) were found to be similar to those reported for ZrO₂(8.1)/MWCNT (Fig. 3). In contrast to what was observed on ZrO₂(8.1)/MWCNT (section 3.2.), the successive NO_x-TPD experiments performed on ZrO₂(6.8)/MWCNT were found to be reproducible, as indicated by the amounts of NO_x released and CO₂ formed in these experiments, 257 ± 6 μmol NO_x/g and 192 ± 5 μmol CO₂/g (Table 1), respectively. The size of the ZrO₂ particles of ZrO₂(6.8)/MWCNT was estimated to be ca. 2.2 nm from the NO_x-TPD data, thus in excellent agreement with the size of the ZrO₂ particles determined by TEM (Table 1). Considering all of the above, these results strongly suggest the absence of carbonaceous deposits on the ZrO₂ particles of ZrO₂(6.8)/MWCNT. Two successive NO_x-TPD experiments were performed on a second aliquot of ZrO₂(6.8)/MWCNT and confirmed the absence of carbonaceous deposits on this particular sample. The reason for the presence of carbonaceous deposits on ZrO₂(8.1)/MWCNT and their absence on ZrO₂(6.8)/MWCNT remains unclear at present. One explanation could stand in the change of the annealing reactor for ZrO₂(6.8)/MWCNT, which may have resulted in differences in the annealing procedure. The measurements performed on the ZrO₂/MWCNT samples in the present study therefore provide further evidence to the robustness and the sensitivity of the NO_x-TPD method. The absence of carbonaceous deposits on ZrO₂(6.8)/MWCNT led us to select this sample as the starting material for the preparation of the tungstated samples studied below.

3.4. WO₃-ZrO₂/MWCNT

Fig. 6 shows XRD patterns for nitric acid treated MWCNT, ZrO₂(6.8)/MWCNT and ZrO₂(6.8)/MWCNT impregnated with three different W loadings. At such a low loading of

ZrO₂, comparison of the blank MWCNT and ZrO₂(6.8)/MWCNT diffraction patterns only shows subtle differences in the $2\theta = 15 - 60^\circ$ range. The most noticeable deviation between ZrO₂(6.8)/MWCNT and the blank MWCNT is between $28 - 38^\circ$ and is likely due to the presence of small ZrO₂ particles. After addition of W to the ZrO₂(6.8)/MWCNT material, more signal is detected between $28 - 38^\circ$ and a shoulder appears at 24° that grows with increasing W loading. WO₃(2.3)-ZrO₂(6.6)/MWCNT and WO₃(4.6)-ZrO₂(6.5)/MWCNT, which contain W loadings lower than that required to achieve a monolayer coverage of ZrO₂ by the tungstates, have very similar diffraction patterns although twice as much W is present in the latter sample. The additional signal in both samples when compared to ZrO₂(6.8)/MWCNT, is most likely a result of diffuse but coherent diffraction from the tungstates. WO₃(8.7)-ZrO₂(6.2)/MWCNT contains above the required amount of W to achieve a monolayer of tungstates and the XRD pattern exhibits a strong shoulder on the MWCNTs diffraction peak at 24° and a peak at 34° that is most likely due to diffraction from WO₃ domains (JCPDS 43-1035), in agreement with the corresponding contributions observed on a WO₃(8.0)/MWCNT sample (not shown) that was synthesized and treated thermally under similar conditions as those described for WO₃(y)-ZrO₂(x)/MWCNT (section 2.1.).

Among the tungstated samples, only WO₃(2.3)-ZrO₂(6.6)/MWCNT was investigated by TEM (Fig. 1h,i). This sample exhibited WO₃-ZrO₂ particles of about 2.4 nm, thus of a size comparable to that of the ZrO₂ particles present on the parent ZrO₂(6.8)/MWCNT composite (Table 1). Characterization methods such as XRD and TEM did not prove to be extraordinarily useful when investigating these complex materials therefore XPS and NO_x-TPD were explored.

XPS measurements found the binding energies of Zr 3d_{5/2} and W 4f_{7/2} to be 182.5 ± 0.1 and 35.7 ± 0.1 eV, respectively, which is in good agreement with the presence of Zr⁴⁺ (zirconia) [40] and W⁶⁺ (tungstates) [37,38,40] species in the samples. Fig. 7 shows the

evolution of the W/Zr atomic ratio determined by XPS as a function of the bulk W/Zr atomic ratio estimated from the ZrO₂ and WO₃ weight loadings of the tungstated samples. It is observed that the W/Zr atomic ratio determined by XPS does not vary linearly (Fig. 7, dotted line) with the known W/Zr atomic ratio of the samples investigated in this study. One explanation to account for this result is that W does not deposit in a highly dispersed state in the series of samples investigated, as is the case for bulk tungstated zirconias for comparable W surface densities, i.e. for W surface densities greater than or equal to that required to achieve monolayer coverage of ZrO₂ by tungstates [36-40]. In the case of the WO₃-ZrO₂/MWCNT materials, tungstates may also deposit onto the MWCNT support as WO₃ nanoparticles with diameters larger than the escape depth of excited electrons from the W 4f transition (~2.63 nm [39]). This would contribute to the deviation of W/Zr atomic ratio measured by XPS from linearity (Fig. 7) despite that monolayer coverage of the ZrO₂ nanoparticles by the tungstates was not achieved. The material complexity therefore makes the use of XPS as a means to probe the coverage of the ZrO₂ nanoparticles by tungstates difficult. In contrast to bulk tungstated zirconias, these XPS data cannot be taken as direct evidence of monolayer coverage of the ZrO₂ nanoparticles by tungstates. To our knowledge, the only method capable of demonstrating monolayer coverage of ZrO₂ by tungstates is NO_x-TPD.

As observed for ZrO₂(6.8)/MWCNT, the two successive NO_x-TPD experiments performed for each tungstated zirconia composite were found to be reproducible (Table 1). Fig. 8 only shows the NO_x and CO₂ profiles recorded in the first NO_x-TPD experiment for each tungstated zirconia composite as the second cycle is nearly identical. As expected from our earlier investigation on bulk tungstated zirconias [27,28] the amount of NO_x released was found to decrease on the introduction of increasing quantities of tungstates (Fig. 9a and Table 2). In parallel, the amount of CO₂ produced was also found to be lower on tungstate

incorporation (Fig. 9b and Table 1). The fact that the amounts of NO_x released, decreased on the introduction of increasing quantities of tungstates indicates that the tungstates interact with the ZrO₂ nanoparticles. The tungstate coverage, defined as the fraction of ZrO₂ covered by tungstates, is estimated with the NO_x-TPD data and found to be 40.2, 64.6 and 77.3 % (Table 2) for WO₃(2.3)-ZrO₂(6.6)/MWCNT, WO₃(4.6)-ZrO₂(6.5)/MWCNT and WO₃(8.7)-ZrO₂(6.2)/MWCNT, respectively.

The theoretical W surface density of the tungstated zirconia composites can be estimated on the basis of their ZrO₂ and WO₃ loadings and considering that the size of the spherical ZrO₂ particles of the ZrO₂(6.8)/MWCNT parent material is 2.2 nm (Fig. 1f,g, Table 1). The method used to determine such a theoretical W density will be detailed for WO₃(2.3)-ZrO₂(6.6)/MWCNT. The specific surface area of spherical ZrO₂ particles with a diameter of 2.2 nm is about 470 m²/g (Table 1). Hence, 1 g of WO₃(2.3)-ZrO₂(6.6)/MWCNT contains 31.2 m² of ZrO₂ and 100.5 μmol of WO₃. The W surface density, which is the ratio of the number of atoms of W to the specific surface of ZrO₂ [28] is therefore deduced to be 1.9 W/nm²_{ZrO₂}. Applying this method to the two other tungstated zirconia composites resulted in theoretical W surface densities of 3.9 and 7.8 W/nm²_{ZrO₂} for WO₃(4.6)-ZrO₂(6.5)/MWCNT and WO₃(8.7)-ZrO₂(6.2)/MWCNT, respectively.

From the difference between the amount of NO_x released from the ZrO₂(6.8)/MWCNT parent material and those released on the tungstated zirconia composites, and the fact that it was found that the addition of 1 W atom prevented the adsorption of 0.77 NO_x molecule in our earlier investigation on bulk tungstated zirconia materials [28], the amount of W interacting with ZrO₂ can be estimated and the corresponding W surface density deduced. This resulted in W surface densities of 1.9, 3.0 and 3.6 W/nm²_{ZrO₂} (Table 2) for WO₃(2.3)-ZrO₂(6.6)/MWCNT, WO₃(4.6)-ZrO₂(6.5)/MWCNT and WO₃(8.7)-ZrO₂(6.2)/MWCNT, respectively. It is remarkable that the W surface density determined by means of the NO_x-

TPD method agrees perfectly with that predicted theoretically for $\text{WO}_3(2.3)\text{-ZrO}_2(6.6)/\text{MWCNT}$ ($1.9 \text{ W/nm}^2_{\text{ZrO}_2}$, Table 2). This indicates that W interacted preferentially with the ZrO_2 particles in this sample. In contrast, the W density was found to be lower than that corresponding to monolayer coverage ($4.1 \text{ W/nm}^2_{\text{ZrO}_2}$ [28]) for the more highly-loaded tungstated samples (Table 2). The fact that the high temperature NO_x desorption peak did not vanish even for the most highly-loaded sample (Fig. 9a) suggests that excess tungsten interacted with MWCNT rather than ZrO_2 and started to form tridimensional WO_3 crystallites in agreement with the XRD data (Fig. 6). Finally, it can be concluded that monolayer coverage of ZrO_2 by W on the studied tungstated zirconia composites is almost complete when introducing W loadings twice as high as that theoretically needed.

5. Conclusions

In this study, the coverage of ZrO_2 nanoparticles supported on MWCNT by carbonaceous deposits or tungstates was investigated. For this purpose, the materials were characterized by NO_x -TPD and these results were combined with XRD, XPS and TEM analyses. It was found that carbon deposition may occur on the ZrO_2 nanoparticles in the course of the synthesis process. These carbonaceous deposits, which covered approximately 30 % of the ZrO_2 surface, can be removed by successive NO_x -TPD experiments, most likely via oxidation by NO_2 released from ZrO_2 . The size of the ZrO_2 particles estimated by NO_x -TPD on $\text{ZrO}_2/\text{MWCNT}$ free of carbonaceous deposits and on a carbon-free $\text{ZrO}_2/\text{MWCNT}$ material were found to be in excellent agreement with that determined by TEM. Incorporation of increasing quantities of W on carbon-free ZrO_2 nanoparticles supported on MWCNT revealed that tungstate coverage of ZrO_2 increased from 40 to 77 % and that W interaction with the ZrO_2 nanoparticles decreased as the amount of W added increased. Remarkably, it was found that W interacted preferentially with the ZrO_2 nanoparticles for a W surface

density of $1.9 \text{ W/nm}^2_{\text{ZrO}_2}$ (half monolayer coverage of the ZrO_2 nanoparticles by tungstates). It was also found that monolayer coverage of ZrO_2 by tungstates on the studied tungstated zirconia composites was nearly complete when introducing W loadings twice as high as that theoretically needed. To our knowledge, these insights into the surface coverage of ZrO_2 by carbon or tungstates could not be obtained by any means other than NO_x -TPD, which makes it a unique method to provide advanced characterization of the surface of oxides supported on MWCNT, in particular, and carbon supports, to a broader general interest.

Acknowledgments

GLH and PRK acknowledge the DOE, Office of Basic Energy Science, Grant No. DE-FG02-01ER15183, for financial support of this research at Yale University/PNNL.

PRK also acknowledges EMSL, a DOE Office of Science User Facility sponsored by the office of Biological and Environmental Research, and Dr. Mark Bowden for assistance collecting the XRD data in this study.

CT acknowledges UPMC and CNRS for providing financial support to this study at the Laboratoire de Réactivité de Surface.

References

- [1] S. Ijima, Helical Microtubules of Graphitic Carbon, *Nature* 354 (1991) 56-58.

- [2] R. Ayranci, G. Baskaya, M. Guzel, S. Bozkurt, M. Ak, A. Savk, F. Sen, Enhanced Optical and Electrical Properties of PEDOT via Nanostructured Carbon Materials: A Comparative Investigation, *Nano Struct. Nano Objects* 11 (2017) 13-19.
- [3] E. Demir, B. Sen, F. Sen, Highly Efficient Pt Nanoparticles and f-MWCNT Nanocomposites Based Counter Electrodes for Dye-Sensitized Solar Cells, *Nano Struct. Nano Objects* 11 (2017) 39-45.
- [4] N. Abdolhi, A. Soltani, H.K. Fadafan, V. Erfani-Moghadam, A.D. Khalaji, H. Balakheyli, Preparation, Characterization and Toxicity Evaluation of Co_3O_4 and NiO-Filled Multi-Walled Carbon Nanotubes Loaded to Chitosan, *Nano Struct. Nano Objects* 12 (2017) 182-187.
- [5] R.S. Rajaura, S. Srivastav, P.K. Sharma, S. Mathur, R. Shrivastava, S.S. Sharma, Y.K. Vijay, Structural and Surface Modification of Carbon Nanotubes for Enhanced Hydrogen Storage Density, *Nano Struct. Nano Objects* 14 (2018) 57-65.
- [6] Y. Ai, L. Liu, K. Jing, L. Qi, Z. Fan, J. Zhou, H-b. Sun, Z. Shao, Q. Liang, Noncovalently Functionalized Carbon Nanotubes Immobilized Fe–Bi Bimetallic Oxides as a Heterogeneous Nanocatalyst for Reduction of Nitroaromatics, *Nano Struct. Nano Objects* 10 (2017) 116-124.
- [7] H-B. Zhang, G-D. Lin, Y-Z. Yuan, Multiwalled Carbon Nanotubes as Novel Support or Promoter of Catalysts, *Current Topics in Catalysis* 4 (2005) 1-21.
- [8] F. Lupo, R. Kamalakaran, C. Scheu, N. Grobert, M. Rülhe, Microstructural Investigations on Zirconium Oxide-Carbon nanotube Composites Synthesized by Hydrothermal Crystallization, *Carbon* 42 (2004) 1995-1999.
- [9] T.Y. Luo, T.X. Liang, C.S. Li, Addition of Carbon Nanotubes During the Preparation of Zirconia Nanoparticles: Influence on Structure and Phase Composition, *Powder Technology* 139 (2004) 118-122.

- [10] Y. Shan, L. Gao, Synthesis and Characterization of Phase Controllable ZrO₂-Carbon nanotube nanocomposites, *Nanotechnology* 16 (2005) 625-630.
- [11] H. Song, X. Qiu, F. Li, Promotion of Carbon Nanotube-Supported Pt Catalyst for Methanol and Ethanol Electro-Oxidation by ZrO₂ in Acidic Media, *Appl. Catal. A: General* 364 (2009) 1-7.
- [12] D-J. Guo, X-P. Qiu, W-T. Zhu, L-Q. Chen, Synthesis of Sulfated ZrO₂/MWCNT Composites as New Supports of Pt Catalysts for Direct Fuel Cell Application, *Appl. Catal. B: Environmental* 89 (2009) 597-601.
- [13] R. Liang, M. Deng, S. Cui, H. Chen, J. Qiu, Direct Electrochemistry and Electrocatalysis of Myoglobin Immobilized on Zirconia/Multi-Walled Carbon Nanotube Nanocomposite, *Mater. Res. Bull.* 45 (2010) 1855-1860.
- [14] S. Lee, Z. Zhang, X. Wang, L.D. Pfefferle, G.L. Haller, Characterization of Multi-Walled Carbon Nanotubes Catalyst Supports by Point of Zero Charge, *Catal. Today* 164 (2011) 68-73.
- [15] C. Liu, S. Lee, D. Su, B. Lee, S. Lee, R.E. Winans, C. Yin, S. Vajda, L. Pfefferle, G.L. Haller, Controlling the Particle Size of ZrO₂ Nanoparticles in Hydrothermally Stable ZrO₂/MWCNT Composites, *Langmuir* 28 (2012) 17159-17167.
- [16] C. Liu, S. Lee, D. Su, Z. Zhang, L. Pfefferle, G.L. Haller, Synthesis and Characterization of Nanocomposites with Strong Interfacial Interactions: Sulfated ZrO₂ Nanoparticles Supported on Multiwalled Carbon Nanotubes, *J. Phys. Chem. C* 116 (2012) 21742-21752.
- [17] C. Liu, L. Pfefferle, G.L. Haller, The Electronic Structure or Charge Delocalization of Sulfated Zirconia (Supported on Multi-Walled Carbon Nanotubes): Acid Sites Probed by X-Ray Absorption Spectroscopy, *Topics Catal.* 57 (2014) 774-784.

- [18] A. Malolepszy, M. Mazurkiewicz, L. Stobinski, B. Lesiak, L. Köver, J. Tóth, B. Mierzwa, A. Borodzinski, F. Nitze, T. Wågberg, Deactivation Resistant Pd-ZrO₂ Supported on Multiwall Carbon Nanotubes Catalyst for Direct Formic Acid Fuel Cells, *Int. J. Hydrogen Energy* 40 (2015) 16724-16733.
- [19] A.K. Baytak, T. Teker, S. Duzmen, M.A. Aslanoglu, Sensitive Determination of Terbutaline in Pharmaceuticals and Urine Samples Using a Composite Electrode Based on Zirconium Oxide Nanoparticles, *Mater. Sci. Eng. C* 67 (2016) 125-131.
- [20] R.S. Amin, A.E. Fetohi, R.M. Abdel Hameed, K.M. El-Khatib, Electrocatalytic Activity of Pt-ZrO₂ Supported on Different Carbon Materials for Methanol Oxidation in H₂SO₄ Solution, *Int. J. Hydrogen Energy* 41 (2016) 1846-1858.
- [21] T. Yamaguchi, Application of ZrO₂ as a Catalyst and a Catalyst Support. *Catal. Today* 20 (1994) 199-218.
- [22] M. Hino, K. Arata, Synthesis of Solid Superacid Catalyst with Acid Strength of H₀ ≤ 16.04, *J. Chem. Soc., Chem. Commun.* 18 (1980) 851-852.
- [23] M. Hino, K. Arata, Synthesis of Solid Superacid of Tungsten Oxide Supported on Zirconia and Its Catalytic Action for Reactions of Butane and Pentane, *J. Chem. Soc., Chem. Commun.* 18 (1988) 1259-1260.
- [24] T. Kim, A. Burrows, C.J. Kiely, I.E. Wachs, Molecular/Electronic Structure–Surface Acidity Relationships of Model-Supported Tungsten Oxide Catalysts, *J. Catal.* 246 (2007) 370-381.
- [25] D. Barton, S.L. Soled, G.D. Meitzner, G.A. Fuentes, E. Iglesia, Structural and Catalytic Characterization of Solid Acids Based on Zirconia Modified by Tungsten Oxide, *J. Catal.* 181 (1999) 57-72.

- [26] V.O. Almeida, N.M. Balzaretto, T.M.H. Costa, M.R. Gallas, Enhanced Mechanical properties in ZrO₂ multi-walled carbon nanotube nanocomposites produced by sol-gel and high-pressure, *Nano Struct. Nano Objects* 4 (2015) 1-8.
- [27] H.Y. Law, J. Blanchard, X. Carrier, C. Thomas, NO_x-TPD as a Tool to Estimate the Accessible Zirconia Surface of ZrO₂-Containing Materials, *J. Phys. Chem. C* 114 (2010) 9731-9738.
- [28] C. Thomas, Should W Surface Density of WO_x-ZrO₂ Catalysts Be Calculated With Respect to the Specific Surface Area of the Sample or That of ZrO₂ Only?, *J. Phys. Chem. C* 115 (2011) 2253-2256.
- [29] W. Zhou, N. Soultanidis, H. Xu, M.S. Wong, M. Neurock, C.J. Kiely, I.E. Wachs, Nature of Catalytically Active Sites in the Supported WO₃/ZrO₂ Solid Acid System: A Current Perspective, *ACS Catal.* 7 (2017) 2181-2198.
- [30] M. Scheithauer, R.K. Grasselli, H. Knözinger, Genesis and Structure of WO_x/ZrO₂ Solid Acid Catalysts, *Langmuir* 14 (1998) 3019-3029.
- [31] D.G. Barton, M. Shtein, R.D. Wilson, S.L. Soled, E. Iglesia, Structure and Electronic Properties of Solid Acids Based on Tungsten Oxide Nanostructures, *J. Phys. Chem. B* 103 (1999) 630-640.
- [32] I.E. Wachs, Raman and IR Studies of Surface Metal Oxide Species on Oxide Supports: Supported Metal Oxide Catalysts, *Catal. Today* 27 (1996) 437-455.
- [33] I.E. Wachs, T. Kim, E.I. Ross, Catalysis Science of the Solid Acidity of Model Supported Tungsten Oxide Catalysts, *Catal. Today* 116 (2006) 162-168.
- [34] T. Kim, A. Burrows, C.J. Kiely, I.E. Wachs, Molecular/Electronic Structure-Surface Acidity Relationships of Model-Supported Tungsten Oxide Catalysts, *J. Catal.* 246 (2007) 370-381.

- [35] N. Vaidyanathan, M. Houalla, D.M. Hercules, Surface Coverage of WO_3/ZrO_2 Catalysts Measured by Ion Scattering Spectroscopy and Low Temperature CO Adsorption. *Surf. Interface Anal.* 26 (1998) 415-419.
- [36] N. Vaidyanathan, D.M. Hercules, M. Houalla, Surface Characterization of WO_3/ZrO_2 Catalysts, *Anal. Bioanal. Chem.* 373 (2002) 547–554.
- [37] M. Valigi, D. Gazzoli, I. Pettiti, G. Mattei, S. Colonna, S. De Rossi, G. Ferraris, WO_x/ZrO_2 Catalysts: Part 1. Preparation, Bulk and Surface Characterization, *Appl. Catal. A: General* 231 (2002) 159-172.
- [38] F. Di Gregorio, V. Keller, Activation and Isomerization of Hydrocarbons Over WO_3/ZrO_2 Catalysts: I. Preparation, Characterization, and X-ray Photoelectron Spectroscopy Studies, *J. Catal.* 225 (2004) 45-55.
- [39] E.I. Ross-Medgaarden, W.V. Knowles, T. Kim, M.S. Wong, W. Zhou, C.J. Kiely, I.E. Wachs, New Insights into the Nature of the Acidic Catalytic Active Sites Present in ZrO_2 -Supported Tungsten Oxide Catalysts, *J. Catal.* 256 (2008) 108-125.
- [40] S. Feng, A. Nagao, T. Aihara, H. Miura, T. Shishido, Selective Hydrogenolysis of Tetrahydrofurfuryl Alcohol on $\text{Pt}/\text{WO}_3/\text{ZrO}_2$ Catalysts: Effect of WO_3 Loading Amount on Activity. *Catalysis Today* (2017), <http://dx.doi.org/10.1016/j.cattod.2017.08.058>.
- [41] G. Ferraris, S. De Rossi, D. Gazzoli, I. Pettiti, M. Valigi, G. Magnacca, C. Morterra, WO_x/ZrO_2 Catalysts: Part 3. Surface Coverage as Investigated by Low Temperature CO Adsorption: FT-IR and Volumetric Studies, *Appl. Catal. A: General* 240 (2003) 119-128.
- [42] K. Pokrovski, K.T. Jung, A.T. Bell, Investigation of CO and CO_2 Adsorption on Tetragonal and Monoclinic Zirconia, *Langmuir* 17 (2001) 4297-4303.

- [43] J. Ni, F.C. Meunier, Esterification of Free Fatty Acids in Sunflower Oil Over Solid Acid Catalysts Using Batch and Fixed Bed-Reactors. *Appl. Catal. A: General* 333 (2007) 122–130.
- [44] K. Suwannakarn, E. Lotero, J.G. Goodwin Jr., C. Lu, Stability of Sulfated Zirconia and the Nature of the Catalytically Active Species in the Transesterification of Triglycerides. *J. Catal.* 255 (2008) 279-286.
- [45] Y-M. Park, J.Y. Lee, S-H. Chung, I.S. Park, S-Y. Lee, D-K. Kim, J-S. Lee, K-Y. Lee, Esterification of Used Vegetable Oils Using the Heterogeneous WO_3/ZrO_2 Catalyst for Production of Biodiesel, *Bioresource Tech.* 101 (2010) S59-S61.
- [46] P. Mongkolbovornkij, V. Champreda, W. Sutthisripok, N. Laosiripojana, Esterification of Industrial-Grade Palm Fatty Acid Distillate over Modified ZrO_2 (with WO_3 , SO_4 and TiO_2): Effects of Co-Solvent Adding and Water Removal, *Fuel Processing Tech.* 91 (2010) 1510–1516.
- [47] F. Cavani, S. Guidetti, C. Trevisanut, E. Ghedini, M. Signoretto, Unexpected Events in Sulfated Zirconia Catalyst During Glycerol-to-Acrolein Conversion, *Appl. Catal. A: General* 409-410 (2011) 267-278.
- [48] I. Dosuna-Rodríguez, C. Adriany, E.M. Gaigneaux, Glycerol Acetylation on Sulphated Zirconia in Mild Conditions, *Catal. Today* 167 (2011) 56-63.
- [49] C-C. Huang, C-J. Yang, P-J. Gao, N-C Wang, C-L. Chen, J-S. Chang, Characterization of an Alkaline Earth Metal-Doped Solid Superacid and Its Activity for the Esterification of Oleic Acid With Methanol, *Green Chem.* 17 (2015) 3609-3620.
- [50] M. Popova, Á. Szegedi, H. Lazarova, A. Ristić, Y. Kalvachev, G. Atanasova, N. Wilde, N. Novak Tušar, R. Gläser, Synthesis of Biomass Derived Levulinate Esters on Novel Sulfated Zr/KIL-2 Composite Catalysts, *Microporous Mesoporous Mater.* 235 (2016) 50-58.

- [51] O. Gorce, F. Baudin, C. Thomas, P. Da Costa, G. Djéga-Mariadassou, On the Role of Organic Nitrogen-Containing Species as Intermediates in the Hydrocarbon-Assisted SCR of NO_x , *Appl. Catal. B: Environmental* 54 (2004) 69-84.
- [52] J. Blanchard, R.P. Doherty, H-Y. Law, C. Méthivier, C. Thomas, On the Detrimental Effect of Tungstates on the $n\text{-C}_{10}$ -SCR of NO_x on $\text{Ag}/\gamma\text{-Al}_2\text{O}_3$, *Topics Catal.* 56 (2013) 134-139.
- [53] T. Bonnotte, R.P. Doherty, C. Sayag, J-M. Krafft, C. Méthivier, M. Sicard, F. Ser, C. Thomas, Insights into the WO_x Coverage-Dependent Location and Oxidation State of Noble Metals Supported on Tungstated Oxides: The Case of $\text{Rh}/\text{WO}_x\text{-Ce}_{0.62}\text{Zr}_{0.38}\text{O}_2$, *J. Phys. Chem. C* 118 (2014) 7386-7397.
- [54] K. Hadjiivanov, V. Avreyska, D. Klissurski, T. Marinova, Surface Species Formed after NO Adsorption and $\text{NO} + \text{O}_2$ Coadsorption on ZrO_2 and Sulfated ZrO_2 : An FTIR Spectroscopic Study, *Langmuir* 18 (2002) 1619-1625.
- [55] B. Tsyntsarsky, V. Avreyska, H. Kolev, Ts. Marinova, D. Klissurski, K. Hadjiivanov, FT-IR Study of the Nature and Reactivity of surface NO_x Compounds Formed after NO adsorption and $\text{NO} + \text{O}_2$ Coadsorption on Zirconia- and Sulfated Zirconia-Supported Cobalt, *J. Mol. Catal. A* 193 (2003) 139-149.
- [56] T. Weingand, S. Kuba, K. Hadjiivanov, H. Knözinger, Nature and Reactivity of the Surface Species Formed after NO Adsorption and $\text{NO} + \text{O}_2$ Coadsorption on a $\text{WO}_3\text{-ZrO}_2$ Catalyst, *J. Catal.* 209 (2002) 539-546.
- [57] F.P.J. Schott, P. Balle, J. Adler, S. Kureti, Reduction of NO_x by H_2 on $\text{Pt}/\text{WO}_3/\text{ZrO}_2$ Catalysts in Oxygen-Rich Exhaust, *Appl. Catal. B* 87 (2009) 18-29.
- [58] B.A.A.L. van Setten, M. Makkee, J.A. Moulijn, Science and Technology of Catalytic Diesel Particulate Filters, *Catal. Rev. Sci. Eng.* 43 (2001) 489-543.

[59] J-O. Müller, B. Frank, R.E. Jentoft, R. Schlögl, D.S. Su, The Oxidation of Soot Particulate in the Presence of NO₂, Catal. Today 191 (2012) 106-111.

Table 1. Summary of the NO_x-TPD and TEM data.

Sample	NO _x - TPD run	CO ₂ μmol/g	NO _x released			Accessible ZrO ₂ surface ^a		ZrO ₂ crystallite size (nm)	
			μmol/g	μmol/g _{ZrO₂}	μmol/g _{ZrO₂}	m ² /g	m ² /g _{ZrO₂}	NO _x -TPD ^b	TEM
MWCNT	1	41	58	-	-	-	-	-	
As-prepared ZrO ₂ (8.1)/MWCNT		-	-	-	-	-	-	2.1	
ZrO ₂ (8.1)/MWCNT	1	164	220	2063	27.8	344	3.0	-	
ZrO ₂ (8.1)/MWCNT	2	186	236	2252	30.4	375	2.8	-	
ZrO ₂ (8.1)/MWCNT	3	218	280	2795	37.7	466	2.2	-	
ZrO ₂ (8.1)/MWCNT	4	210	286	2874	38.8	479	2.2	2.3	
MWCNT	1	54	74	-	-	-	-	-	
MWCNT	2	54	66	-	-	-	-	-	
ZrO ₂ (6.8)/MWCNT	1	188	263	2901	32.9	483	2.1	-	
ZrO ₂ (6.8)/MWCNT	2	192	251	2735	31.0	456	2.3	-	
ZrO ₂ (6.8)/MWCNT	3	197	257	2826	32.0	471	2.2	2.2	
WO ₃ (2.3)-ZrO ₂ (6.6)/MWCNT	1	118	171	1622	17.9	270	-	-	
WO ₃ (2.3)-ZrO ₂ (6.6)/MWCNT	2	124	180	1751	19.4	292	-	2.4	
WO ₃ (4.6)-ZrO ₂ (6.5)/MWCNT	1	78	127	991	10.7	165	-	-	
WO ₃ (4.6)-ZrO ₂ (6.5)/MWCNT	2	79	127	1004	10.9	167	-	-	
WO ₃ (8.7)-ZrO ₂ (6.2)/MWCNT	1	59	99	640	6.6	107	-	-	
WO ₃ (8.7)-ZrO ₂ (6.2)/MWCNT	2	55	96	579	6.0	97	-	-	

^avalues estimated by considering a NO_x surface density of 6 μmol/m²_{ZrO₂} [27,28]

^bvalues estimated by considering spherical particles and a ZrO₂ density of 5.8 x 10⁶ g/m³

Table 2. Tungstate coverage and W surface density of the $\text{WO}_3(y)\text{-ZrO}_2(x)\text{/MWCNT}$ samples estimated from NO_x -TPD data

Sample	Tungstate coverage (%)	NO_x released $\mu\text{mol NO}_x/\text{g}_{\text{ZrO}_2}$	W density ($\text{W}/\text{nm}^2_{\text{ZrO}_2}$)	
			Theoretical ^a	Estimated ^b
MWCNT	-	-	-	-
$\text{ZrO}_2(6.8)\text{/MWCNT}$	-	2821	-	-
$\text{WO}_3(2.3)\text{-ZrO}_2(6.6)\text{/MWCNT}$	40.2	1687	1.9	1.9
$\text{WO}_3(4.6)\text{-ZrO}_2(6.5)\text{/MWCNT}$	64.6	998	3.9	3.0
$\text{WO}_3(8.7)\text{-ZrO}_2(6.2)\text{/MWCNT}$	77.3	640	7.8	3.6

^acalculated on the basis of the loadings of ZrO_2 and WO_3 in the samples, and considering a mean ZrO_2 particle size of 2.2 nm ($470 \text{ m}^2/\text{g}_{\text{ZrO}_2}$, Table 1)

^b based on the amount of NO_x released from the $\text{ZrO}_2(6.8)\text{/MWCNT}$ parent sample and those released on the tungstated zirconia composites, and considering that the addition of 1 W atom prevented the adsorption of 0.77 NO_x molecules [28]

Figure Captions

Fig. 1. TEM micrographs and particle size distributions of (a) MWCNT, (b) and (c) as-prepared $\text{ZrO}_2(8.1)/\text{MWCNT}$, (d) and (e) $\text{ZrO}_2(8.1)/\text{MWCNT}$ submitted to 4 successive NO_x -TPD experiments, (f) and (g) $\text{ZrO}_2(6.8)/\text{MWCNT}$ submitted to 3 successive NO_x -TPD experiments, (h) and (i) $\text{WO}_3(2.3)\text{-ZrO}_2(6.6)/\text{MWCNT}$ submitted to 2 successive NO_x -TPD experiments. The scale bar is 10 nm in each micrograph.

Fig. 2. NO_x (magenta), NO_2 (red), NO (blue) and CO_2 (green) profiles obtained on 0.1399 g of MWCNT, after annealing the sample at 500 °C for 2 h in 100 $\text{mL}_{\text{NTP}}/\text{min}$ of He and RT exposure to 230 $\text{mL}_{\text{NTP}}/\text{min}$ of $\text{NO}_x(400 \text{ ppm})\text{-O}_2(8\%)\text{-He}$ for about 160 min followed by temperature-programmed desorption from RT to 420 °C (3 °C/min) in 230 $\text{mL}_{\text{NTP}}/\text{min}$ of He. (For interpretation of the references to color in figure legend, the reader is referred to the web version of the article.)

Fig. 3. NO_x and CO_2 profiles obtained in successive NO_x -TPD experiments (a) 1st NO_x -TPD, (b) 2nd NO_x -TPD, (c) 3rd NO_x -TPD, (d) 4th NO_x -TPD on 0.1515 g of $\text{ZrO}_2(8.1)/\text{MWCNT}$, after annealing of the sample at 500 °C for 2 h in 100 $\text{mL}_{\text{NTP}}/\text{min}$ of He and RT exposure to 230 mL /min of $\text{NO}(400 \text{ ppm})\text{-O}_2(8\%)\text{-He}$ for about 190 min followed by temperature-programmed desorption from RT to 370 °C (3 °C/min) in 230 $\text{mL}_{\text{NTP}}/\text{min}$ of He. It must be noted that the He flow during the annealing step between the 3rd and the 4th NO_x -TPD was set to 230 $\text{mL}_{\text{NTP}}/\text{min}$ at 150 °C. (For interpretation of the references to color in figure legend, the reader is referred to the web version of the article.)

Fig. 4. (a) NO_x and (b) CO₂ profiles obtained in successive NO_x-TPD experiments: 1st NO_x-TPD (blue), 2nd NO_x-TPD (red), 3rd NO_x-TPD (magenta), 4th NO_x-TPD (green) on 0.1515 g of ZrO₂(8.1)/MWCNT, after annealing of the sample at 500 °C for 2 h in 100 mL_{NTP}/min of He and RT exposure to 230 mL/min of NO(400 ppm)-O₂(8%)-He for about 190 min followed by temperature-programmed desorption from RT to 370 °C (3 °C/min) in 230 mL_{NTP}/min of He. Please note that the He flow during the annealing step between the 3rd and the 4th NO_x-TPD was set to 230 mL_{NTP}/min at 150 °C and the corresponding CO₂ trace was recorded (black). (For interpretation of the references to color in figure legend, the reader is referred to the web version of the article.)

Fig. 5. NO_x and CO₂ profiles obtained in successive NO_x-TPD experiments (a) 1st NO_x-TPD, (b) 2nd NO_x-TPD, (c) 3rd NO_x-TPD on 0.1155 g of ZrO₂(6.8)/MWCNT, after annealing of the sample at 500 °C for 2 h in 100 mL_{NTP}/min of He and RT exposure to 230 mL_{NTP}/min of NO(400 ppm)-O₂(8%)-He for about 180 min followed by temperature-programmed desorption from RT to 380 °C (3 °C/min) in 230 mL_{NTP}/min of He. (For interpretation of the references to color in figure legend, the reader is referred to the web version of the article.)

Fig. 6. XRD data for MWCNT (green), ZrO₂(6.8)/MWCNT (black), WO₃(2.3)-ZrO₂(6.6)/MWCNT (red), WO₃(4.6)-ZrO₂(6.5)/MWCNT (purple) and WO₃(8.7)-ZrO₂(6.2)/MWCNT (blue) annealed at 450 °C, vertical lines in inset represent WO₃ (solid, 23.2, 29.2 and 33.3°) and ZrO₂ (dashed, 30.1 and 34.9°). All spectra are scaled to the intensity of the (002) diffraction of MWCNT, equivalent to referencing to the same amount of MWCNT. (For interpretation of the references to color in figure legend, the reader is referred to the web version of the article.)

Fig. 7. W/Zr atomic ratio determined by XPS as a function of the nominal W/Zr atomic ratio for the $\text{WO}_3(y)\text{-ZrO}_2(x)\text{/MWCNT}$ samples.

Fig. 8. NO_x and CO_2 profiles obtained in the 1st NO_x -TPD experiment on (a) $\text{WO}_3(2.3)\text{-ZrO}_2(6.6)\text{/MWCNT}$, (b) $\text{WO}_3(4.6)\text{-ZrO}_2(6.5)\text{/MWCNT}$, (c) $\text{WO}_3(8.7)\text{-ZrO}_2(6.2)\text{/MWCNT}$, after annealing of the sample at 500 °C for 2 h in 100 mL_{NTP}/min of He and RT exposure to 230 mL_{NTP}/min of $\text{NO}(400 \text{ ppm})\text{-O}_2(8\%)\text{-He}$ for about 180 min followed by temperature-programmed desorption from RT to 380 °C (3 °C/min) in 230 mL_{NTP}/min of He. (For interpretation of the references to color in figure legend, the reader is referred to the web version of the article.)

Fig. 9. (a) NO_x and (b) CO_2 profiles obtained in the 1st NO_x -TPD experiment on $\text{ZrO}_2(6.8)\text{/MWCNT}$ (black), $\text{WO}_3(2.3)\text{-ZrO}_2(6.6)\text{/MWCNT}$ (red), $\text{WO}_3(4.6)\text{-ZrO}_2(6.5)\text{/MWCNT}$ (purple), $\text{WO}_3(8.7)\text{-ZrO}_2(6.2)\text{/MWCNT}$ (blue) and MWCNT (green) after annealing of the sample at 500 °C for 2 h in 100 mL_{NTP}/min of He and RT exposure to 230 mL_{NTP}/min of $\text{NO}(400 \text{ ppm})\text{-O}_2(8\%)\text{-He}$ for about 180 min followed by temperature-programmed desorption from RT to 380 °C (3 °C/min) in 230 mL_{NTP}/min of He. (For interpretation of the references to color in figure legend, the reader is referred to the web version of the article.)

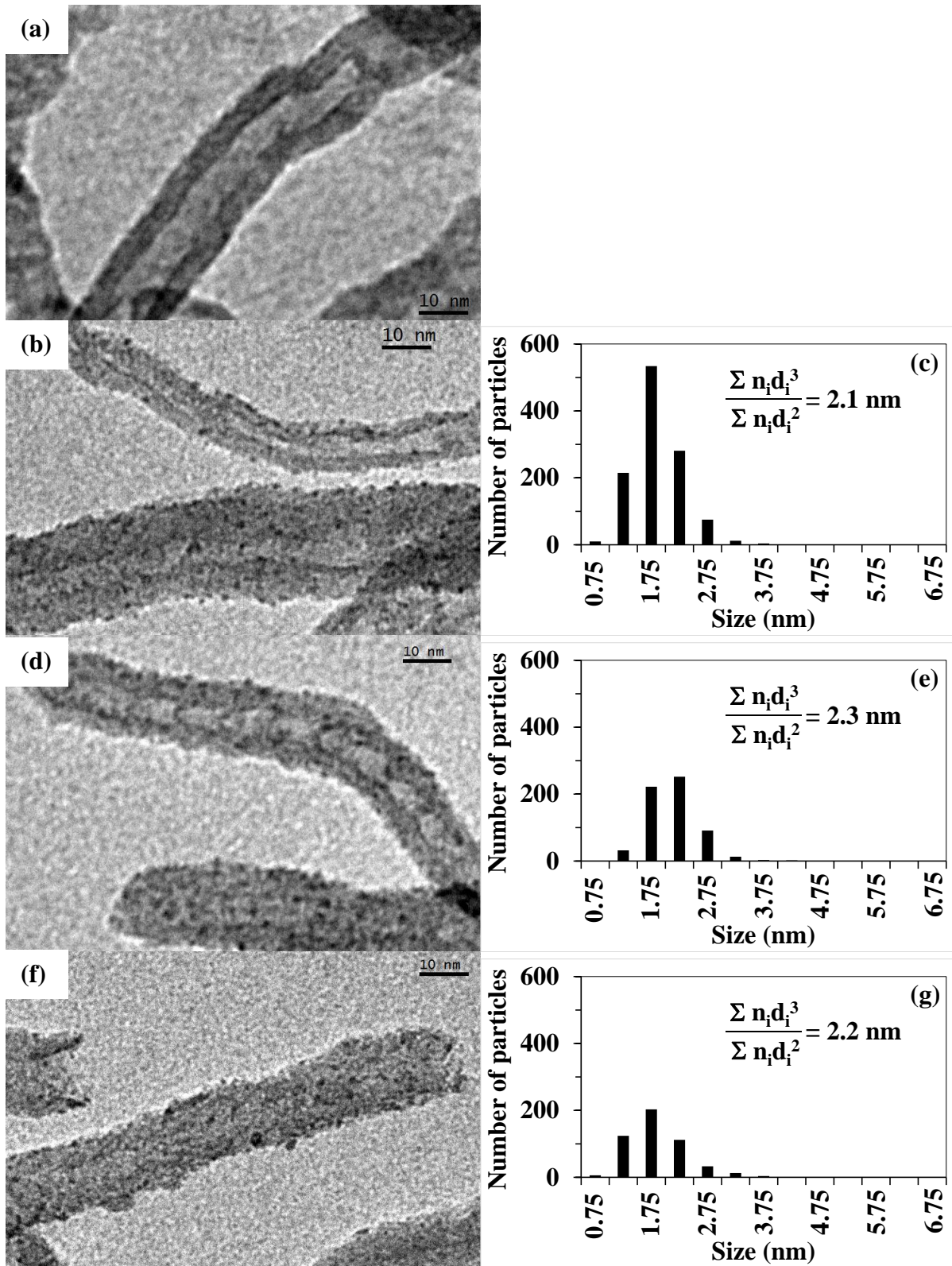


Fig .1 (continued)

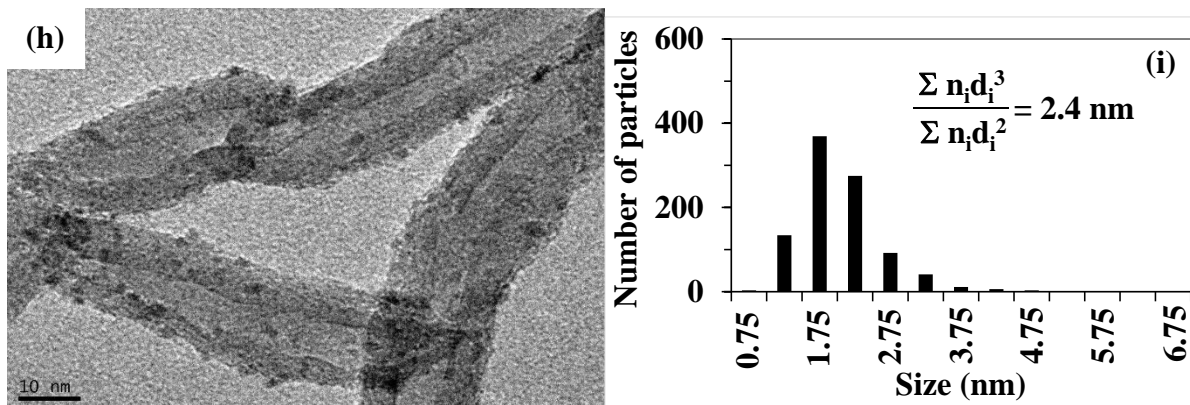


Fig. 1

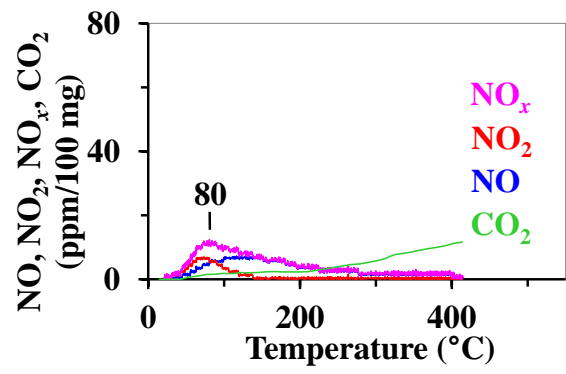


Fig. 2

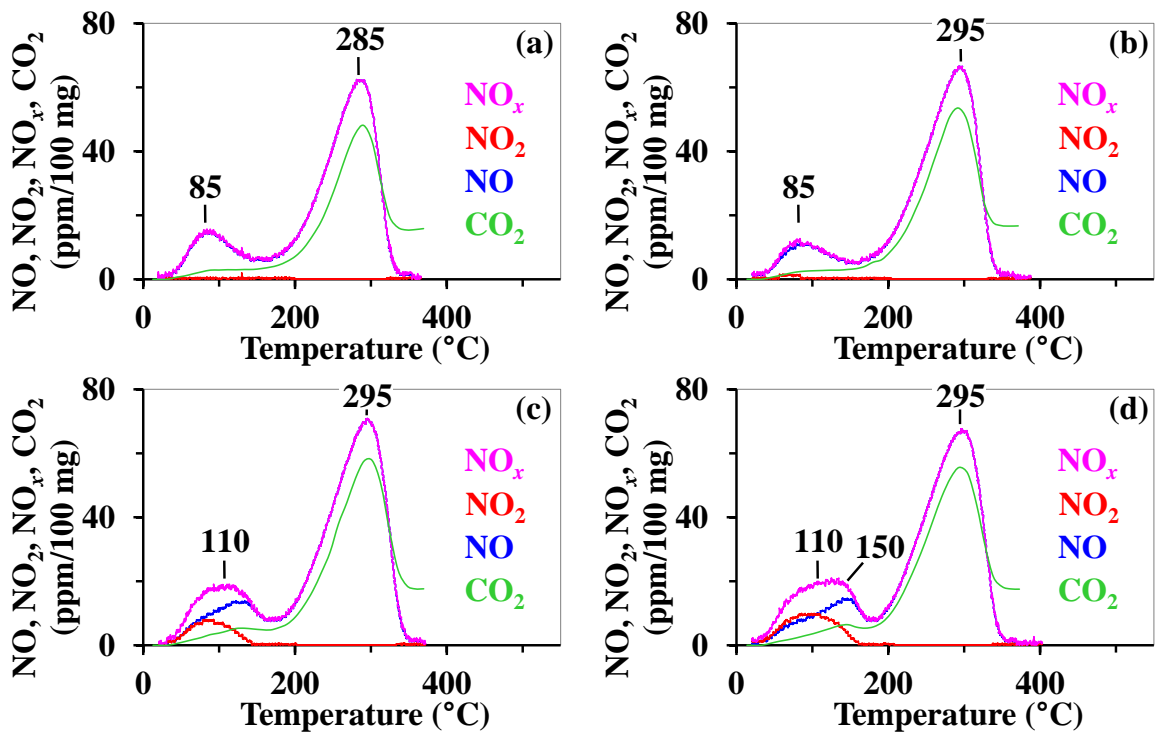


Fig. 3.

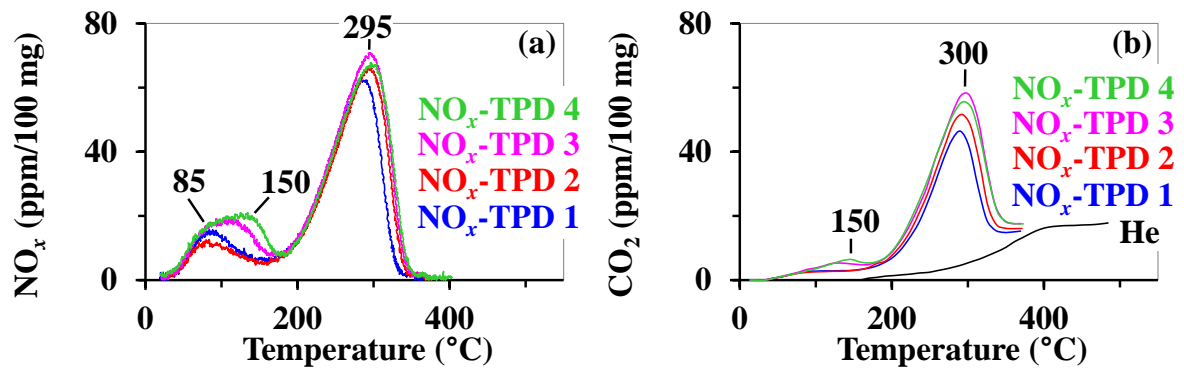


Fig. 4.

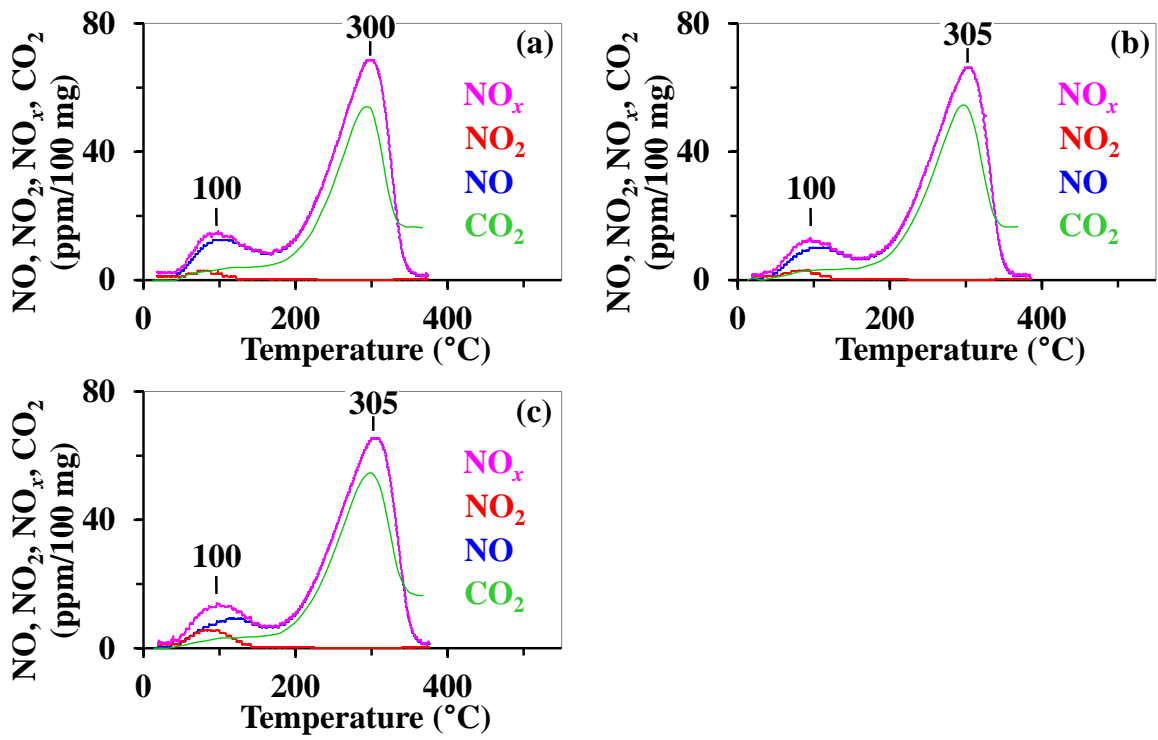


Fig. 5.

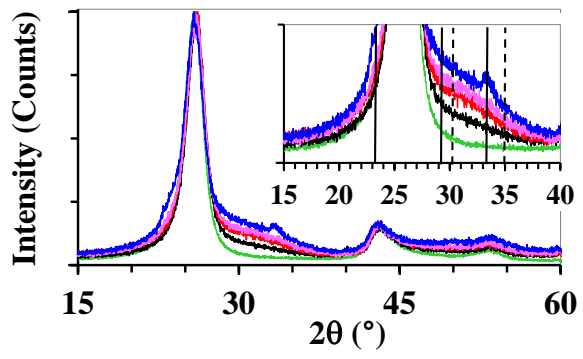


Fig. 6.

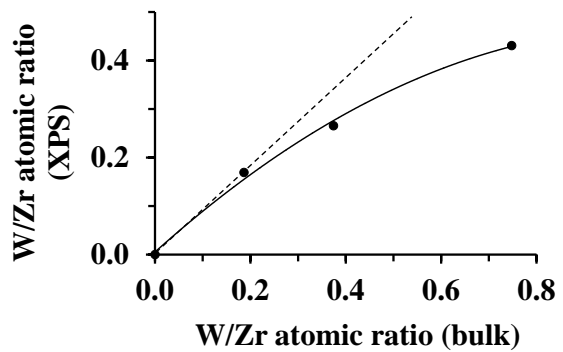


Fig. 7.

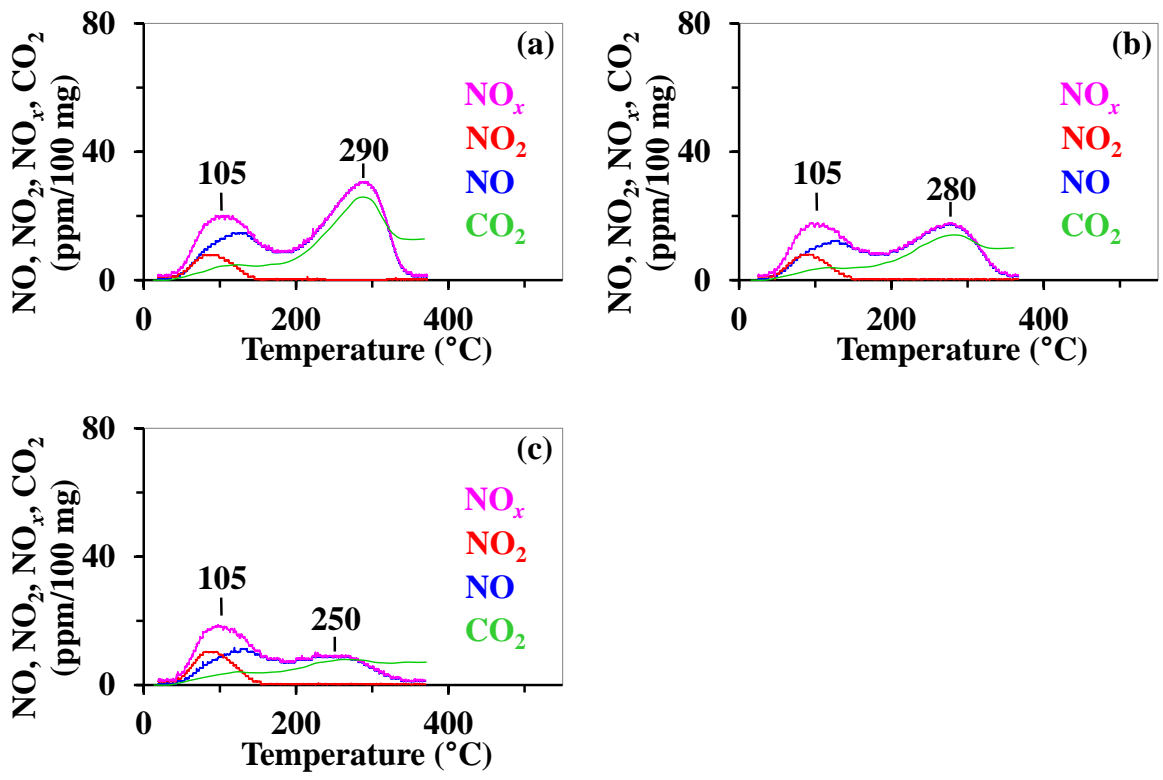


Fig. 8.

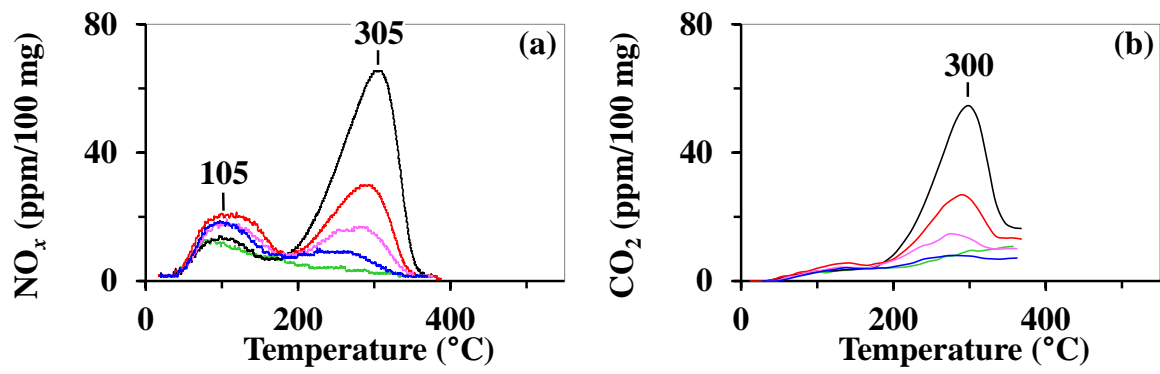


Fig. 9.